
This is an electronic reprint of the original article.
This reprint may differ from the original in pagination and typographic detail.

Mai, Cuc Thi Kim; Halme, Janne; Nurmi, Heikki A.; da Silva, Aldeliane M.; Lorite, Gabriela S.; Martineau, David; Narbey, Stéphanie; Mozaffari, Naeimeh; Ras, Robin H.A.; Hashmi, Syed Ghufan; Vuckovac, Maja

Super-Droplet-Repellent Carbon-Based Printable Perovskite Solar Cells

Published in:
Advanced Science

DOI:
[10.1002/adv.202401016](https://doi.org/10.1002/adv.202401016)

Published: 10/07/2024

Document Version
Publisher's PDF, also known as Version of record

Published under the following license:
CC BY

Please cite the original version:
Mai, C. T. K., Halme, J., Nurmi, H. A., da Silva, A. M., Lorite, G. S., Martineau, D., Narbey, S., Mozaffari, N., Ras, R. H. A., Hashmi, S. G., & Vuckovac, M. (2024). Super-Droplet-Repellent Carbon-Based Printable Perovskite Solar Cells. *Advanced Science*, 11(26), Article 2401016. <https://doi.org/10.1002/adv.202401016>

This material is protected by copyright and other intellectual property rights, and duplication or sale of all or part of any of the repository collections is not permitted, except that material may be duplicated by you for your research use or educational purposes in electronic or print form. You must obtain permission for any other use. Electronic or print copies may not be offered, whether for sale or otherwise to anyone who is not an authorised user.

Super-Droplet-Repellent Carbon-Based Printable Perovskite Solar Cells

Cuc Thi Kim Mai,* Janne Halme,* Heikki A. Nurmi, Aldeliane M. da Silva, Gabriela S. Lorite, David Martineau, Stéphanie Narbey, Naeimeh Mozaffari, Robin H. A. Ras, Syed Ghufran Hashmi, and Maja Vuckovac*

Despite attractive cost-effectiveness, scalability, and superior stability, carbon-based printable perovskite solar cells (CPSCs) still face moisture-induced degradation that limits their lifespan and commercial potential. Here, the moisture-preventing mechanisms of thin nanostructured super-repellent coating (advancing contact angle $>167^\circ$ and contact angle hysteresis 7°) integrated into CPSCs are investigated for different moisture forms (falling water droplets vs water vapor vs condensed water droplets). It is shown that unencapsulated super-repellent CPSCs have superior performance under continuous droplet impact for 12 h (rain falling experiments) compared to unencapsulated pristine (uncoated) CPSCs that degrade within seconds. Contrary to falling water droplets, where super-repellent coating serves as a shield, water vapor is found to physisorb through porous super-repellent coating (room temperature and relative humidity, RH 65% and 85%) that increase the CPSCs performance for 21% during ≈ 43 d similarly to pristine CPSCs. It is further shown that water condensation forms within or below the super-repellent coating (40 °C and RH 85%), followed by chemisorption and degradation of CPSCs. Because different forms of water have distinct effects on CPSC, it is suggested that future standard tests for repellent CPSCs should include rain falling and condensate formation tests. The findings will thus inspire the development of super-repellent coatings for moisture prevention.

increases in power conversion efficiency (PCE) from 3.8%^[1] to 26.1%.^[2] These cells offer a low-cost and scalable production method, making them a promising photovoltaic (PV) technology for various applications, including grid-scale electricity generation^[3-7] and integration into light-harvesting systems for indoor environments.^[8-10] However, despite these advancements, PSCs currently face challenges related to long-term operational stability^[11-13] under diverse environmental conditions, largely attributed to the degradation of hybrid metal halide perovskite light absorbers when exposed to moisture.^[14-19]

Efforts to address moisture-related degradation in PSCs have focused on encapsulation methods or incorporating moisture barrier layers. While the glass-glass encapsulation method has effectively prevented moisture degradation, its complex and costly nature poses challenges, particularly for large-scale applications and flexible devices.^[20] An alternative approach utilizes hydrophobic coatings with a water contact angle $>90^\circ$ ^[21,22] to passivate the PSC

surface and repel water.^[23,24] These coatings reduce the contact area between water droplets and solid surfaces, inhibiting moisture ingress and potential damage to the PSC. However, despite the improved PSC stability (summarized in Table S1, Supporting

1. Introduction

Solution-processed perovskite solar cells (PSCs) have undergone significant advancements in recent years, with notable

C. T. K. Mai, A. M. da Silva, G. S. Lorite, S. G. Hashmi
Microelectronics Research Unit
Faculty of Information Technology & Electrical Engineering
University of Oulu
Pentti Kaiteran katu 1, Oulu 90570, Finland
E-mail: thi.mai@oulu.fi

J. Halme, H. A. Nurmi, R. H. A. Ras, M. Vuckovac
Department of Applied Physics
Aalto University School of Science
Konemiehentie 1, Espoo 02150, Finland
E-mail: janne.halme@aalto.fi; maja.vuckovac@aalto.fi
H. A. Nurmi, R. H. A. Ras, M. Vuckovac
Centre of Excellence in Life-Inspired Hybrid Materials (LIBER)
Aalto University
Espoo, Finland
D. Martineau, S. Narbey
Solaronix SA
Rue de l' Ouriette 129, Aubonne CH-1170, Switzerland
N. Mozaffari
Department of Materials Science and Engineering
Monash University
Clayton, Victoria 3800, Australia

 The ORCID identification number(s) for the author(s) of this article can be found under <https://doi.org/10.1002/advs.202401016>

© 2024 The Authors. Advanced Science published by Wiley-VCH GmbH. This is an open access article under the terms of the [Creative Commons Attribution](#) License, which permits use, distribution and reproduction in any medium, provided the original work is properly cited.

DOI: 10.1002/advs.202401016

Information),^[20,25–34] hydrophobic coatings, usually applied as thick and densely packed films (such as poly(ethylene oxide) (PEO), Teflon, and photocurable fluoropolymers), can crack or peel off during heating–cooling cycles when exposed to environmental conditions, resulting in lead leakage and less efficient heat dissipation out of the cell under high illuminations.^[35]

Recently, thin hydrophobic and superhydrophobic (advancing contact angles $>150^\circ$ and contact angle hysteresis $<10^\circ$ ^[21,22,36]) coatings applied via spray-coating^[35] and spin-coating^[37] methods have emerged as a cost-effective solution and have been shown to improve the stability of PSCs effectively^[35] (summarized in Table S1, Supporting Information).^[35,38,39] However, these coatings are very fragile (lack mechanical durability)^[40] and easily damaged when exposed to environmental conditions such as the high impact of falling rain droplets. Additionally, their water repellency degrades over time,^[41] reducing their efficiency in moisture prevention. Furthermore, studies on moisture-preventing mechanisms of these coatings and their effectiveness under practical environmental conditions such as rain falling and condensate formation are scarce. Moreover, the standard aging tests that engage different moisture (water) forms and proper wetting characterization are lacking.

Here, we successfully integrated super-repellent colloidal dispersion of hydrophobic silica nanoparticles (commercially available Glaco coating) into CPSCs, which resulted in advancing contact angle, $\theta_{adv} >167^\circ$ and contact angle hysteresis, CAH $<10^\circ$. We further studied moisture-induced degradation mechanisms of this porous, thin, and transparent super-repellent coating in the presence of different moisture forms (bulk water vs vapor vs condensed droplets). We showed that super-repellent coating can shield against bulk water, making them remarkably stable for 12 h under constant droplet impact (rain falling experiments) compared to pristine (uncoated) CPSCs that degraded within seconds. We demonstrate that super-repellent coating allows vapor physisorption at room temperature, improving CPSCs performances for ≈ 43 d while the condensate formation due to super-saturated vapor (when temperatures are elevated from 23°C to 40°C and RH 85%) leads to degradation. Thus, we propose rain falling and condensate formation experiments as additional aging tests for hydrophobic and superhydrophobic PSCs. Successful thin super-repellent coating must pass rain falling and condensate formation tests to qualify as a moisture-protective coating.

2. Results and Discussion

2.1. Unencapsulated Super-Repellent Carbon-Based Printable Perovskite Solar Cells

We use CPSCs with Glass/FTO/c-TiO₂/mp-TiO₂/mp-ZrO₂/carbon/infiltrated perovskite structure^[42] that have shown great stability when unencapsulated and exposed to a humid environment.^[43] The compact TiO₂ (c-TiO₂) layer is deposited using spray pyrolysis, while mesoporous layers of TiO₂ (mp-TiO₂), ZrO₂ (mp-ZrO₂), and carbon are fabricated via screen-printing. A perovskite precursor solution of methylammonium lead iodide (MAPbI₃) and 5-ammonium valeric acid iodide (5-AVAI) is infiltrated throughout the electrode stack using a programmable multi-channel pipetting robot (Solaronix). The samples are an-

nealed at 55°C for 90 min and then cooled to room temperature to form perovskite crystals in the porous electrode structure (Figure 1a). These unencapsulated CPSCs are denoted as pristine CPSCs. Contact angle measurement (Figure 1b) shows their hydrophilic nature ($\theta < 90^\circ$) with advancing contact angle, $\theta_{adv} = 53^\circ$, receding contact angle $\theta_{rec} = 14^\circ$ and contact angle hysteresis $\theta_{adv} - \theta_{rec} = 39^\circ$ (for definitions, see Supporting Information). During contact angle measurements, the pristine CPSC turns yellow, showing fast degradation when it comes in contact with macroscopic droplets ($\approx 8\ \mu\text{L}$) (Video S1, Supporting Information). As expected, scanning electron microscopy (SEM) imaging shows porous carbon nanoparticles and graphite flakes (Figure 1c).

To achieve super-repellency, we introduce a thin transparent layer (Figure S1, Supporting Information) of hydrophobic silica nanoparticles (commercially available Glaco Mirror Coat Zero) (Figure 1d), and these CPSCs are denoted as super-repellent CPSCs. The coating was applied directly on the carbon layer using a spin-coater, and one- versus three-layer coating was explored to achieve the best water repellence. Compared to the pristine CPSCs (Figure 1b), we found a massive improvement in repellence for three-layer coating, as both θ_{adv} and θ_{rec} increase to 167° and 160° , respectively (Figure 1e) and contact angle hysteresis decreases to 7° . The SEM image reveals full and homogeneous coverage with silica nanoparticles (Figure 1f), consistent with EDS mapping of Si element for super-repellent CPSC (Figure S2, Supporting Information).

The effect of the coating layer was further studied with an oscillating droplet tribometer (ODT, see Experimental Section and Supporting Information for details)^[44,45] that probes droplet mobility by measuring friction forces that water-like ferrofluid droplets experience when moving on a repellent surface (Figure 1g). Despite the low CAH (obtained with contact angle measurements) for both one- and three-layer coated CPSCs, the droplets were immobile (pinned) on one-layer coated samples (Video S2, Supporting Information), indicating large friction forces due to less or non-uniform coverage of hydrophobic silica nanoparticles, resulting in weakly repellent CPSCs (Figure 1g). This further implies no droplet bouncing on weakly-repellent CPSCs. On the other hand, the droplet was highly mobile for three-layer coated samples (Video S3, Supporting Information), experiencing friction forces of $710 \pm 26\ \text{nN}$ typical for super-repellent surfaces^[46,47] (Figure 1h). This indicates sufficient coverage with a three-layer coating that allows droplet bouncing (Video S4, Supporting Information). Thus, the following discussion will be based on the unencapsulated three-layer coated super-repellent CPSCs.

2.2. Photovoltaic (PV) Performance of Super-Repellent CPSCs

To investigate how super-repellent coating is integrated into CPSC, we examined unencapsulated CPSCs (34 Batch I and 16 Batch II) by measuring their PV parameters (Figure S3, Supporting Information) before (pristine) and after applying coating (super-repellent). To provide more reliable and realistic results, we perform current–voltage (J – V) measurements on all CPSCs (an active area of $1.5\ \text{cm}^2$) using large aperture area of $0.64\ \text{cm}^2$. By reducing the aperture area from 0.64 to $0.14\ \text{cm}^2$, the PCE

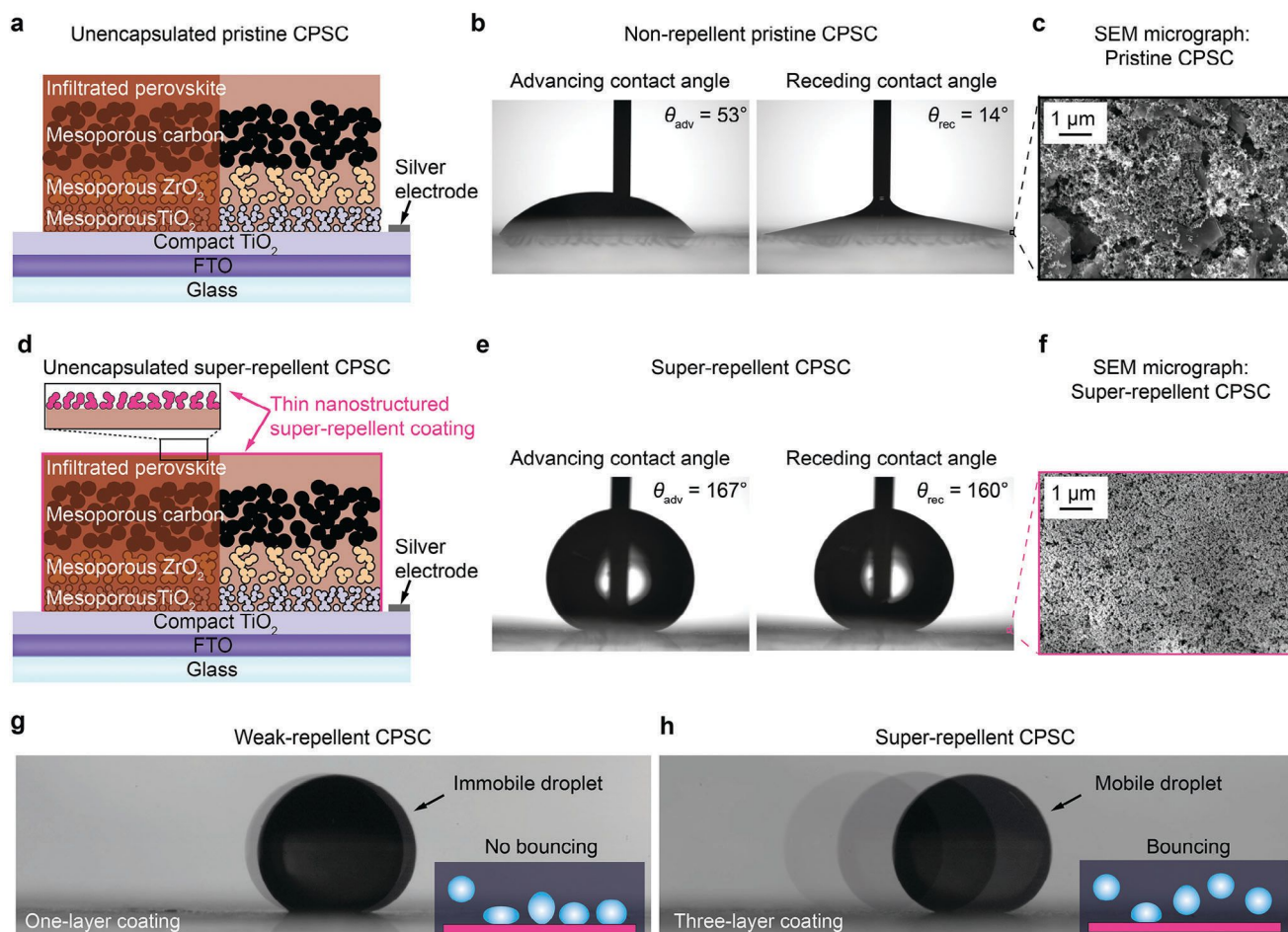


Figure 1. Unencapsulated carbon-based printable perovskite solar cells (CPSC): Pristine versus super-repellent CPSCs. a) Schematic illustration of pristine CPSC (noncoated) showing the layered stack structure: FTO glass, a thin layer of compact TiO_2 , and the mesoporous layers (TiO_2 , ZrO_2 , and carbon electrode) infiltrated with perovskite with its b) wetting properties (measured advancing and receding contact angles) and c) scanning electron microscopy (SEM) micrograph (top view). d) Schematic illustration of super-repellent CPSC coated with a thin nanostructured super-repellent coating (commercially available Glaco) with its e) wetting properties (measured advancing and receding contact angles) and f) SEM micrograph (top view). g,h) Video frames captures from oscillation droplet tribometer measurements showing g) immobile ferrofluid droplet on one-layer coated CPSC indicating no droplet bouncing (weak-repellent CPSC) and h) highly mobile ferrofluid droplet on three-layer coated CPSC resulted in droplet bouncing.

values of the reverse scan increase from $\approx 8\%$ up to $\approx 11\%$ (Figure S3, Supporting Information). Then we coated the CPSCs with the super-repellent coating (17 from Batch I and 8 from Batch II) and measured their PV parameters after applying the coating. The measured power conversion efficiency (PCE) for pristine CPSCs (before coating) and super-repellent CPSCs (after coating) (17 of each from Batch I) is shown in Figure 2a, while all PV parameters are shown in Figure S4 (Supporting Information).

We found average PCE of pristine CPSCs and super-repellent CPSCs to be almost identical (pristine CPSCs is $7.2\% \pm 0.3\%$, and for super-repellent CPSCs $7.3\% \pm 0.2\%$), giving no statistically significant differences in the PCE when applying the super-repellent coating (t-test with 95% confidence) (Table S2, Supporting Information), with the representative J - V curves shown in Figure 2b. The bump in the reverse scan is characteristic of devices featuring mesoporous interfacial and insulating layers, such as dye-sensitized solar cells and mesoporous perovskite solar cells, such as CPSCs.^[48–52] This phenomenon is primarily at-

tributed to interface charge accumulation and release of interfacial charges during voltage sweeps, which results in an additional current compared to the typical response. We performed experiments with a relatively low scan rate of 4.2 mV s^{-1} and to mitigate the potential overestimation of the fill factor (FF) and PCE caused by the expansion of the reverse-scan J - V curve, we report the average PCE derived from both forward and reverse scans for all the devices. The average photocurrent density (J_{SC}) and open circuit voltage (V_{OC}) showed a statistically significant effect of super-repellent coating with a p-value less than 0.05 (Table S2, Supporting Information). However, the effect size was insignificant, with a change of less than 5% (Table S2, Supporting Information).

The data presented in Figure 2b demonstrate that the shapes and slopes of the J - V curves, particularly near V_{OC} , are identical for both types of cells. This uniformity suggests no significant difference in the series resistance (R_s), which indicates the conductivity of the carbon layer. We thus found that the coating does not affect the conductivity of the carbon electrode.

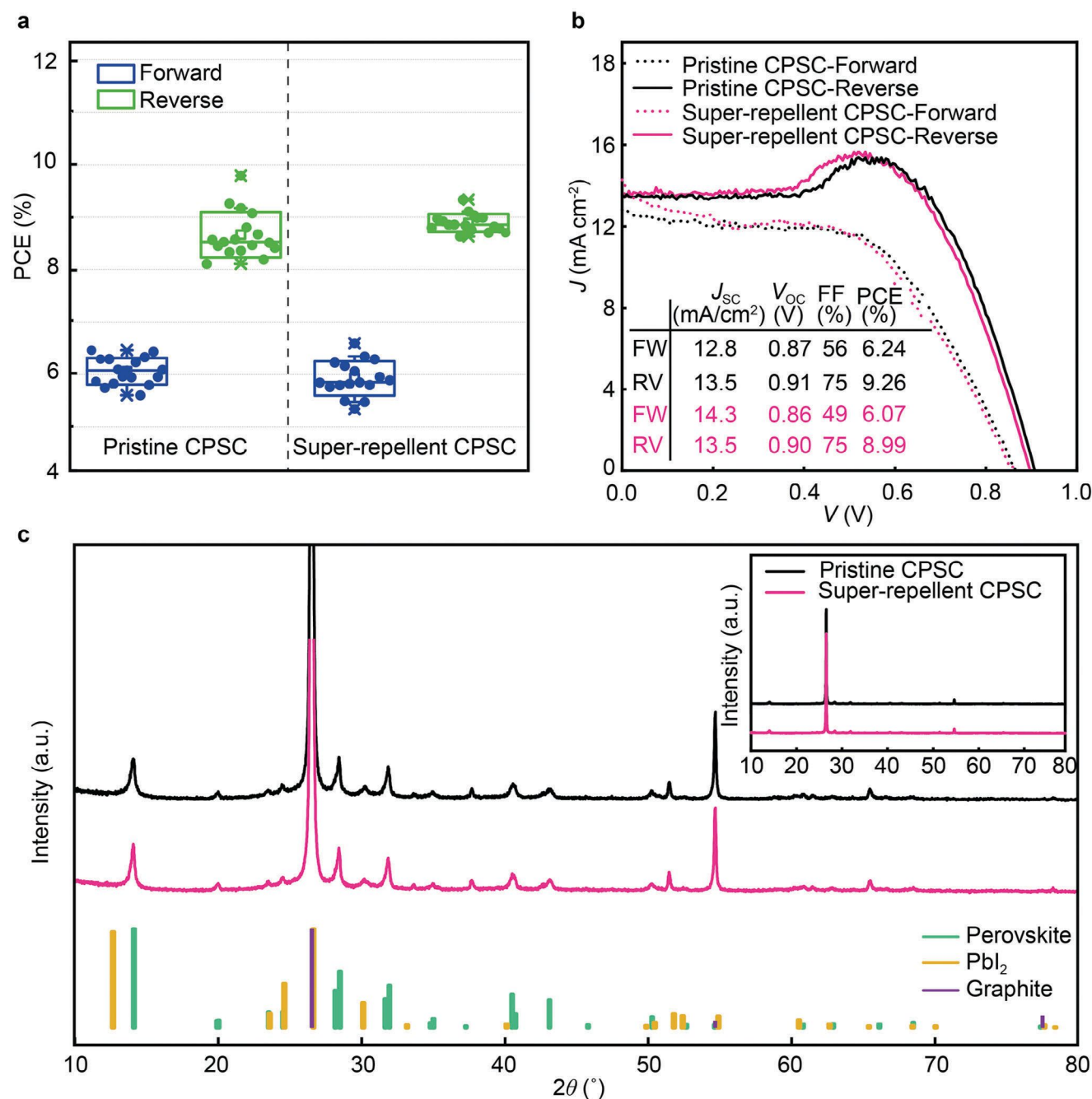


Figure 2. Integration of super-repellent coating into CPSC. a) Statistical PCE for both forward and backward scans for 17 unencapsulated CPSCs before applying coating (pristine) and the same CPSC after applying coating (super-repellent CPSCs) (from Batch I). b) J-V curves of representative pristine and super-repellent CPSCs with a measured aperture area of 0.64 cm² under 1 Sun condition. c) XRD patterns of pristine and super-repellent CPSC. Note that no additional peaks characteristic to super-repellent coating (hydrophobic silica nanoparticles) were found primarily due to the amorphous structure of the coating.

Therefore, the applied super-repellent coating did not cause any significant changes in the performance or composition of CPSCs. This was further confirmed by XRD measurements (Figure 2c), which showed no effect on the perovskite crystal structure as the d-spacing and the intensity of peaks remained constant after the coating application. Also, no new PbI₂ peak was formed for super-repellent CPSCs. Thus, an excellent inte-

gration of super-repellent coating has been achieved. The results from Batch II confirmed that the coating did not impact initial PV performance and showed excellent reproducibility of the application process (Figure S5 and Table S3 in Supporting Information). In this work, we do not aim to improve PCE through synthesis but to explore the effect of super-repellent coating on CPSCs performances and how the coating performs in the

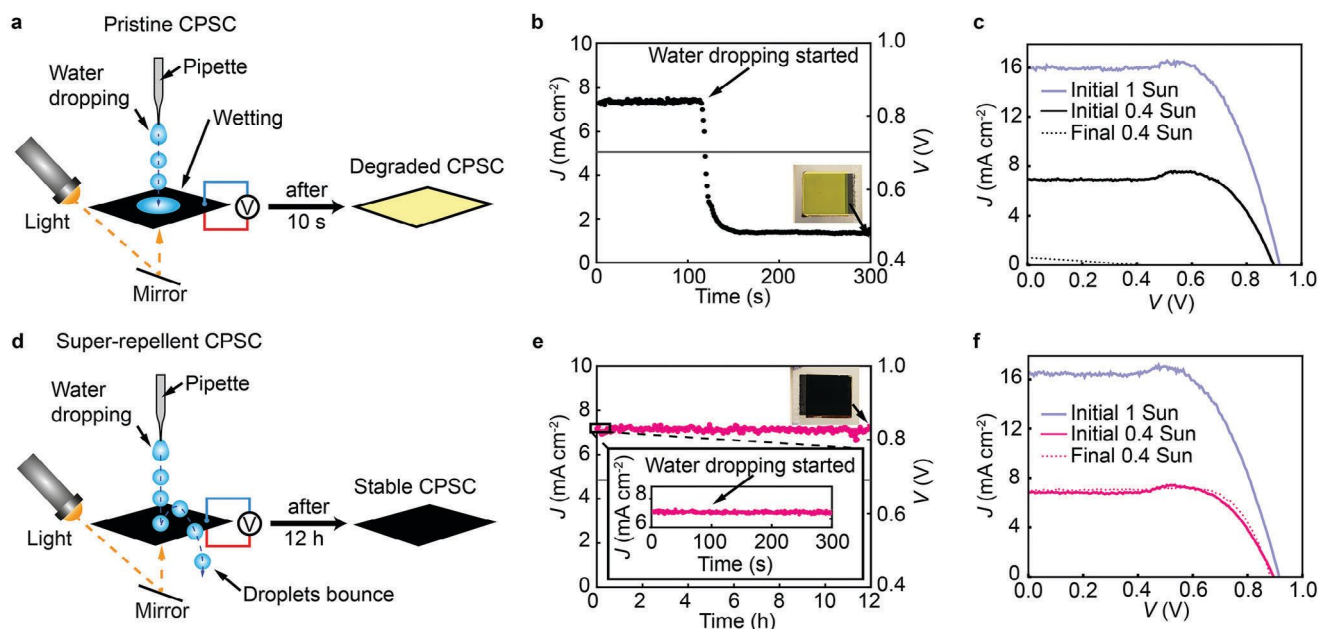


Figure 3. Rain falling experiments. a) Schematic illustration of the setup showing pipette for water dropping (rain falling experiments), light, and mirror for sunlight simulation. Due to strong wetting, the pristine CPSC degraded in 10 s after water dropping started. The PV parameters were measured simultaneously. b) Current density versus time for pristine CPSC under illumination (0.4 Sun) and bias 0.695 V (V_{MPP}). c) J - V curves of the pristine CPSC at the initial 1 and 0.4 Sun (attenuated due to the reflection through a mirror) and after the water dropping test under 0.4 Sun. d) Schematic illustration of the setup for super-repellent CPSC showing droplet bouncing mechanism due to high repellency resulting in stable PCSC even after 12 h. e) Current density versus time of super-repellent CPSC under illumination (0.4 Sun) and bias 0.67 V (V_{MPP}). f) J - V curves of super-repellent CPSC with the same parameters from (c). The active area was 0.64 cm² (achieved by using a mask). The shapes and slopes of the J - V curves near V_{oc} in (c) and (f) are identical for pristine and super-repellent CPSCs, indicating that the coating does not affect the conductivity of the carbon electrode.

presence of different moisture forms (falling water droplets vs water vapor vs condensed droplets).

2.3. Performance of Super-Repellent CPSC in the Presence of Different Moisture Forms

2.3.1. Super-Repellent CPSC in Rain Conditions

To investigate how super-repellent coating behaves as a moisture barrier for bulk water, we performed rain falling experiments (Figure 3, Videos S5–S7, Supporting Information). The rain falling experiments were done by continuous dropping of the droplets with a pipette from 2 cm height and the frequency of ≈ 3 drops per second on the horizontally placed CPSCs with carbon electrodes facing up (back side) at 30–40% initial relative humidity (RH). Simulated sunlight is irradiated on the glass side (front side) of the CPSCs by the mirror reflection, and the intensity of the incident light was attenuated to approximately 0.4 Sun. Besides the light irradiation, the mirror was also used to simultaneously observe the moment of degradation in CPSCs (color changes to yellow, Video S5, Supporting Information). The PV performance of CPSCs during the rain falling experiment was continuously monitored. The photocurrent density was recorded with Zahner potentiostat at the voltage corresponding to the maximum power point (V_{MPP}) under approximately 0.4 Sun (Figure 3b,e). It is noted that the obtained photocurrent density is comparable to the photocurrent current at maximum power

point (J_{MPP}) achieved with J - V characterization as shown in Table S4 (Supporting Information).

The current density of pristine CPSC sharply decreased in only 10 s after exposure to macroscopic water droplets (Figure 3a,b), which matched the rapid color change from black to yellow (Figure S6 and Video S5, Supporting Information). This indicates quick decomposition of the perovskite absorber, resulting in cell damage and declined performance (Figure 3c and Table S4, Supporting Information). In contrast, the current density of super-repellent CPSC stays remarkably stable at the maximum power point voltage (V_{MPP}) throughout 12 h of exposure to macroscopic water droplets (Figure 3d,e) without degradation in cell appearance (Video S6, Supporting Information) and PV performance (Figure 3f and Table S4, Supporting Information). The superior performance of super-repellent CPSC is due to a low CAH and small friction forces that enable highly mobile droplets. The droplets thus easily bounce off the super-repellent CPSC (Video S7, Supporting Information), reducing the contact time (between droplet and CPSC) and protecting the CPSC from water-induced damage. Thus, a thin layer of super-repellent coating serves as a remarkably stable shield under the impact of $\approx 130\,000$ droplets and blocks the mass transfer of water.

2.3.2. Super-Repellent CPSC in a Humid Environment

To study the vapor-induced degradation in a humid environment, we performed the dark storage aging test at room temperature

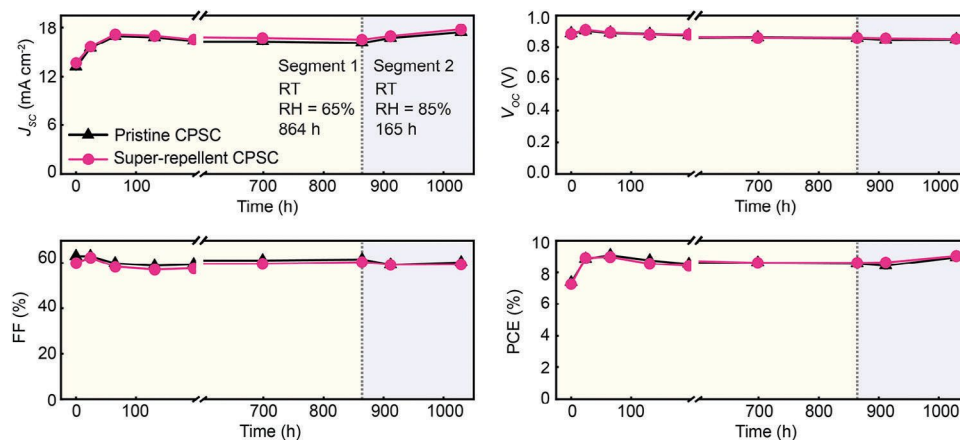


Figure 4. Dark storage test at room temperature (RT) and relative humidity (RH) 65% and 85%. Evolution of average (of forward and reverse scans) PV parameters of unencapsulated pristine and super-repellent CPSCs (6 cells in each group) under 1 Sun (aperture area of 0.64 cm²). The aging test consists of two segments: segment 1 was conducted at RT and 65% RH for 864 h, and segment 2 was conducted at RT, 85% RH for 165 h. The presented values are average values for six different cells from each group. The distribution of PV parameters after each segment is reported in Figure S7 (Supporting Information).

(RT) and relative humidity (RH) 65% and 85%. One set of 12 unencapsulated CPSCs (Batch I, 6 pristine CPSCs, and 6 super-repellent CPSCs), was placed in an automated environmental chamber (VCL 4006, Vötsch Industrietechnik, Germany) at the RT (23 °C) and the RH of 65% and 85% for specific durations (Figure 4). During the aging test, the carbon electrode was facing up to expose CPSCs to the humid environment fully, and PV parameters were monitored throughout 1029 h (Figure 4).

The initial average PCE values for pristine and super-repellent CPSCs were almost identical (pristine CPSCs $7.4 \pm 0.1\%$ and super-repellent CPSCs $7.3 \pm 0.1\%$) as well as the other PV parameters (Table S5, Supporting Information) confirming excellent integration of super-repellent coating. The overall behavior of these CPSCs was observed for ≈ 43 d. In the first 65 h (of denoted segment 1, Figure 4), the average PCE significantly increased by 23% compared to the initial values (Figure 4 and Table S6, Supporting Information). This was followed by a slight decrease in average PCE (during 864 hours) and then with its final increase (after 864 hours, end of segment 1) of $15.9\% \pm 2.8\%$ (pristine CPSCs) and $18.5\% \pm 1.7\%$ (super-repellent CPSCs) compared to initial PCE (Figure 4, and Table S6, Supporting Information). The overall PCE improvement is mainly due to increased photocurrent (the open circuit voltage and fill factor remain stable).

Interestingly, with increasing RH to 85% in segment 2 (Figure 4), the photocurrent and PCE of both pristine and super-repellent CPSCs recovered (Figure 4). After 165 hours of segment 2, the average PCE increased (compared to the initial value) by $21.5\% \pm 3.2\%$ for pristine CPSCs and $24.5\% \pm 3.4\%$ for super-repellent CPSCs (Table S6, Supporting Information). Surprisingly, the enhanced PCE at relatively high humidity (i.e., 65% and 85%) was maintained during 1029 h, not only for super-repellent CPSCs but also for unencapsulated pristine CPSCs. The enhancement in photocurrent and PCE for pristine CPSCs can be attributed to the interaction with humidity.^[43,53–56] In CPSCs, the hydrophobic carbon electrode can block the large water droplets that might be produced under high-humidity conditions, and only allows the gaseous vapor to pass, enabling per-

ovskite crystal growth without causing damage to its chemical structure.^[43] This also further enhances the interface between perovskite and different layers of the printed stack.^[43,56] Since the same was observed for liquid-repellent CPSCs (same evolution behavior, no statistically significant differences in the average change percentage of PV parameters, except for the fill factor (FF), Table S7, Supporting Information), we can conclude that the eventual performance enhancement of super-repellent CPSCs is mainly due to the porous structure of the super-repellent coating (Figure 1f). Contrary to the bulk water (Figure 5a), where the water droplets are repelled (due to low CAH and friction forces, droplets bounce off the CPSCs), in a humid environment, it allows the water vapor to penetrate through the pores (Figure 5b). It thus absorbs a small vapor concentration (physisorption), resulting in perovskite crystal growth with preferential orientation and increasing the efficiency of CPSCs.

2.3.3. Super-Repellent CPSC in Supersaturating Vapor

To study the stability of super-repellent CPSCs in supersaturating vapor, we performed an aging test at elevated temperature on the same CPSCs from the previous aging test in the environmental chamber. The CPSCs were placed in the chamber with RH of 85% and RT, and the temperature was increased from 23 °C to 40 °C (keeping constant RH). At the beginning of the experiment, we noticed water condensation on the carbon electrode due to reached supersaturation (supersaturated air with RH >100%). The supersaturation happened due to the temperature difference between the CPSCs and the environmental chamber.^[57] When the air warms up to $T_{air} = 40$ °C (during the time Δt_{air}), there is a delay in warming up of CPSC ($\Delta t_{CPSC} > \Delta t_{air}$) due to the low heat transfer rate^[58] of air and the larger heat capacity^[58] of the CPSC (solid) compared to air (Figure 5f). Thus, the sample temperature falls behind the air ($\Delta T = T_{air} - T_{CPSC}$), and consequently, the humidity in the sample increases. This becomes more significant going from the sample surface to its depth (the core of the

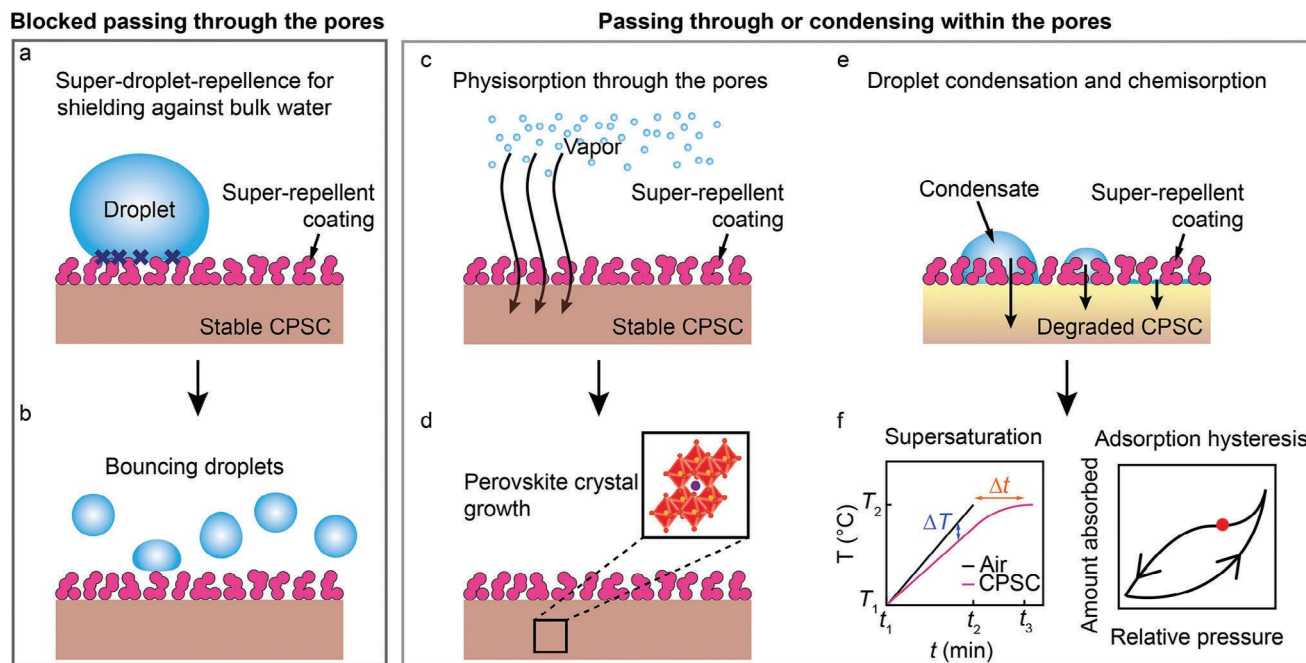


Figure 5. Repelling mechanisms for different moisture (water) forms. a) Schematic illustration of shielding against bulk water showing blockage of mass transfer and resulting b) droplet bouncing from the super-repellent CPSC. c) Schematic illustration of vapor absorption through the pores of the coating resulting in (d) perovskite crystal growth. e) Schematic illustration of condensation on super-repellent CPSC shows condensate growth within (or even below) the coating. f) The graphs for supersaturation conditions and adsorption hysteresis characteristic of condensation from supersaturated vapor. The supersaturation graph shows the warm-up curve for air and CPSC indicated time delay Δt of CPSC to reach the air temperature and temperature difference ΔT at which supersaturation occurs. After the CPSC equilibrate to air temperatures ($\Delta T = 0$) and RH 85%, due to adsorption hysteresis the amount of condensed water inside the sample does not decrease to the same amount during adsorbing water in the warm-up time (e.g., stays at the position indicated with the red dot).

sample is colder than its surface during the warming-up time). Due to this, the RH at the CPSC reaches a value higher than 100%, and macroscopic condensation occurs, which is more severe inside the CPSC than on its surface. This results in significant liquid water condensation inside the CPSC, causing chemisorption and degradation of CPSC (color changes to yellow). When the sample finally equilibrates to the air temperature (40 °C) and humidity 85%, due to adsorption hysteresis (Figure 5f), the amount of condensed water inside the sample does not decrease to the same amount during physisorption (water absorption in the warm-up time).^[59] This was confirmed with J - V measurements after 48 h of exposure to 40 °C and RH of 85%. The pristine and super-repellent CPSCs show degradation in PCE of $61.7\% \pm 10.0\%$ and $55.2\% \pm 15.9\%$, respectively, compared to the values before the test (Figure S8 and Tables S8–S10, Supporting Information). It is worth to note that the super-repellent coating is stable at elevated temperatures, verifying by imaging with an atomic force microscope (AFM) (Figure S9, Supporting Information). The AFM imaging was done by heating/cooling cycles (65 °C/RT, 85 °C/RT, and 100 °C/RT), showing coating roughness unchanged through all cycles (Figure S9, Supporting Information). Nevertheless, the coating does not affect the degradation rate of the super-repellent CPSCs under high-temperature conditions. This was demonstrated by a dark storage test at 65 °C in ambient for another set of 12 CPSCs (Batch I, 6 pristine CPSCs, and 6 super-repellent CPSCs) using a thermal chamber (Mettler, Germany). After 981 h of test-

ing, the PCE of encapsulated pristine and super-repellent CPSCs reduced $35.3\% \pm 2.2\%$ and $33.8\% \pm 2.9\%$ of the initial values, respectively, with no statistically significant differences in the average change percentage between the two types of cells (Figure S10 and Tables S11–S13, Supporting Information).

To validate this further, we performed condensation tests (Batch II, 6 pristine, and 6 super-repellent CPSCs) in a homemade humidity chamber (Figure S11, Supporting Information). After the supersaturation, the droplets condensed on the CPSCs (approximately after 30 min, Figure S11, Supporting Information), and we continued condensation studies for 90 min more (2 h total). There was a clear difference in the density of condensed droplets and their sizes between pristine and super-repellent CPSCs (Figure S11, Supporting Information). The droplets formed on super-repellent CPSCs were smaller, less spread, and less dense compared to pristine CPSCs, which is attributed to the higher θ_{adv} . As explained earlier, the coating could not prevent the CPSCs from degradation as expected for thin transparent nanoporous super-repellent coatings. Even in the case of repellent material, it is expected to fail in fogging experiments due to its porosity, as the tiny condensed droplets form within or below the coating. As droplets grow, they form sticky droplets that do not have enough energy to jump off the coating (Figure S11, Supporting Information). These smaller condensates further serve as favorable points to accumulate water and behave like hydrophilic material, similar to pristine CPSCs (Figure 1b). Similar phenomena were observed on tilted surfaces of the

pristine and super-repellent glass slides (Figure S12, Supporting Information). While the average PCE of super-repellent CPSCs dropped to $0.1 \pm 0.1\%$ (for pristine CPSCs to $0.4 \pm 0.5\%$) (Figure S13 and Table S14, Supporting Information), the super-repellent coating remained stable after the condensation test and elevated temperatures (was not damaged) as it was able to repel droplets (Video S8, Supporting Information).

3. Conclusion

In summary, we focused on understanding the moisture-preventing mechanisms of thin nanostructures super-repellent coating from different moisture forms (falling water droplets vs water vapor vs condensed water droplets). To tackle this, we successfully integrated super-repellent coating (commercially available Glaco) into carbon-based printable perovskite solar cells (CPSCs) and tested its performance in conditions that resemble the outdoor environment: rain conditions, humid environment, and supersaturating vapor. The coating demonstrated remarkable success in repelling water droplets, effectively preventing simulated rain-induced damage and contributing to the longevity of the CPSCs. The coating allows for the physisorption of water vapor in humid environments, enhancing the performance of super-repellent CPSCs (similar to pristine CPSCs). In supersaturating vapor, condensation occurs within and below the coating due to the temperature difference between the CPSC and air in the environment, followed by the chemisorption and degradation of CPSCs. In general, thin nanoparticle coatings, despite particle size, maintain porosity, which leads to failure in the condensation test for CPSCs due to droplet formation inside the coating or on the perovskite surface. Porosity poses a significant challenge for transparent thin repellent coatings, necessitating exploration of non-porous microstructure roughness layers that could prevent droplet contact with perovskite, although integration requires careful consideration to avoid solvent-related degradation during fabrication. Thus, rain falling and condensate formation tests are crucial aging tests for future hydrophobic/superhydrophobic coatings development as they provide a key understanding of the interaction mechanisms of different forms of moisture with coating. The findings are significant for the field as implementing hydrophobic and superhydrophobic (water-repellent) coatings as a moisture-preventing barrier is becoming an emerging research direction. We anticipate our findings inspire the development of repellent coatings that prevent unwanted water condensation and chemisorption.

4. Experimental Section

Materials: Fluorine-doped tin oxide (FTO)-coated glass substrate (Product code: TCO22-7/LI), Ti-Nanoxide T165/SP, Zr-Nanoxide ZT/SP, and Elcocarb B/SP and perovskite precursor solution containing methylammonium lead iodide (MAPbI₃) and 5-ammonium valeric acid iodide (5-AVAI) was purchased from Solaronix, Switzerland. Titanium diisopropoxide bis (acetylacetonate, 75% in isopropanol) was purchased from Sigma-Aldrich. The super-repellent coating is Glaco Mirror Coat Zero (SOFT99).

Device Fabrication: Unencapsulated Devices: Fluorine-doped tin oxide (FTO)-coated glass substrate (10 cm x 10 cm, $7 \Omega \text{ Sq}^{-1}$) was etched with an automated fiber laser to fabricate individual cell electrodes followed with ultrasonic cleaning in 1% Hellmanex aqueous solution, ace-

tone, and isopropanol solvents (15 min each). A thin (30–50 nm) compact TiO₂ layer (c-TiO₂) was then deposited on an active area (through a glass mask) by aerosol spray pyrolysis at 450 °C using titanium diisopropoxide bis (acetylacetonate, 75% in isopropanol) dissolved in absolute ethanol (1:80 v/v) as precursor and oxygen as carrier gas. After cooling to room temperature (RT), mesoporous TiO₂ (400–600 nm), the insulating mesoporous ZrO₂ (1–2 μm), and the conductive porous carbon (10–12 μm) layers were deposited via sequentially screen-printing Ti-Nanoxide T165/SP, Zr-Nanoxide ZT/SP, and Elcocarb B/SP pastes layer by layer. After each screen-printing step, the printed layers were dried at 150 °C for 5 min before sintering. Sintering temperatures for mp-TiO₂ and mp-ZrO₂ layers were 500 °C for 30 min, while the porous carbon layer was 400 °C for 30 min to form the mesoporous triple-layer-based scaffold. After final sintering, the printed layers were cooled to RT. The perovskite precursor solution (Solaronix) was prepared by mixing lead iodide (1.2 M), methylammonium iodide (1.2 M), 5-ammonium valeric acid iodide (5% mol) and dissolving in gamma-butyrolactone and ethanol mixture (85:15 v/v). The solution was stirred on a preheated (70 °C) hot plate for 30 min. The warm, clear yellow solution was filtered through a 0.2 μm PTFE filter and cooled to room temperature. The solution was then deposited using a programmable multichannel pipetting robot (Solaronix) on an as-fabricated substrate masked with polyimide cut-out shapes (Impregnation Masks, Solaronix). The wet substrates were allowed to dwell for several minutes to let the liquid sip into the porous structure. The perovskite crystals in the porous electrode structure were achieved with final annealing in an oven at 55 °C for 90 mins. For encapsulation procedure, see Supporting Information.

The 50 PSCs were prepared as described above, of which 34 CPSCs are from Batch I, and 16 CPSCs are from Batch II.

Super-Repellent Coating Application: The superhydrophobic coating was prepared using Glaco Mirror Coat Zero, a commercial product of a colloidal suspension of hydrophobic silica nanoparticles in isopropanol. To achieve an efficient super-repellent layer, the spin-coating of Glaco was done directly on the carbon electrode of CPSCs, masked with Kapton tape to avoid spreading the solution on the nonactive area of device. 0.2 mL solution was deposited using a three-step sequential spin coating method: 2000 rpm (90 s), 4000 rpm (40 s), and 3000 rpm (60 s), followed by annealing on a preheated (70 °C) hotplate for 10 mins (one-layer coating). The procedure is repeated three times to ensure full coverage (three-layer coating).

Device Characterization: Photovoltaic Measurements: The current–voltage (J–V) curves of CPSCs were acquired using a Keithley 2401 Source Meter under simulated AM 1.5G sunlight at 1000 W m⁻² (1 Sun) irradiance generated by a Xenon-lamp-based solar simulator (Pecell Technologies, PEC-L01, Japan) with the intensity calibrated with a reference photovoltaic cell AK-300 (Konica Minolta, Japan). The scan range from –0.1 to 1 V and scan rate 4.2 mV s⁻¹ were applied to measure the devices covered with masks with apertures of 0.14 and 0.64 cm² to define active areas.

Scanning Electron Microscopy (SEM): The SEM imaging was done using field-emission scanning electron microscopy (FESEM, Zeiss ULTRA plus).

XRD Measurements: The XRD measurements were carried out using the same procedures described in the previous report.^[37] The XRD data was measured using a Rigaku Smartlab diffractometer with Cu anode and Ge (220) double bounce monochromator.

UV/Vis Spectroscopy: The reflectance of the fabricated CPSCs was measured with an integrated sphere in a UV/Vis/NIR Spectrometer (Lambda 950, Perkin Elmer).

Atomic Force Microscopy (AFM): The surface morphology and stability of the samples under different temperatures were performed with a Bruker Multimode 8 atomic force microscope (AFM) with a high-temperature stage for sample heating. The system was coupled with the thermal applications controller (TAC) from Bruker to control the temperature of the heat stage and the probe. A pyramidal silicon probe with a cantilever spring constant of 0.3 N m⁻¹ (HQ-CSC37/Al BS, MikroMasch) was used. The topography images were acquired with NanoScope software using ScanAsyst (Peak Force Tapping) imaging mode from Bruker. Images of 5 μm x 5 μm with 256 x 256 pixels were acquired at a scan rate of 1.0 Hz and a peak

force frequency of 2 kHz. First, the measurements were performed at room temperature (RT), after which the stage and the probe were heated at 65 °C, 85 °C, and 100 °C. Before increasing the temperature, the system was set back to RT in each imaging cycle. For each temperature, a set of 5 images was acquired after at least 30 min for stabilization. Image processing and root mean square (RMS) roughness measurements were performed with Gwyddion software.

Contact Angle Goniometry (CAG): Contact angles were measured using a conventional optical tensiometer (Attension Theta, Biolin Scientific) following the established protocol.^[60] Advancing contact angles were measured by placing a 0.22 μL droplet on the surface and increasing its volume to 20 μL , with 0.025 $\mu\text{L s}^{-1}$. Then, an additional 20 μL was added, and receding contact angles were measured by decreasing droplet volume with 0.025 $\mu\text{L s}^{-1}$. The data were analyzed using Young-Laplace fitting with OneAttension software, and reported advancing and receding contact angles were those when the droplet baseline increased and decreased, respectively.

Oscillating Droplet Tribometry (ODT): Friction forces for moving droplets on super-repellent CPSCs were measured using ODT^[44,45] as follows. A 5 μL water-like ferrofluid droplet (0.2 vol% nanoparticles) was placed on the CPSCs by pipette and brought into oscillations by moving the magnets in a sinusoidal fashion. The motion was captured with a Phantom V1610 high-speed camera at 1000 fps. The droplet position was tracked and fitted to the analytical solution for harmonic oscillations to obtain the friction force. For more details, see Supporting Information.

Supporting Information

Supporting Information is available from the Wiley Online Library or from the author.

Acknowledgements

This work was supported by the Jane and Aatos Erkkö Foundation and Technology Industries of Finland Centennial Foundation for CAPRINT project funding (#2430354811), European Research Council grant ERC-2016-CoG (725513-SuperRepel) and Academy of Finland Center of Excellence Program (2022-2029) in Life-Inspired Hybrid Materials (LIBER) (#346109). G.S.L. acknowledges the support received from the Academy of Finland (#320090 and #317437). C.T.K.M. acknowledges Optoelectronics and Measurement Techniques (OPEM) Research Unit, University of Oulu, for permitting the use of the humidity chamber (Model VCL 4006, Vötsch Industrietechnik, Germany).

Conflict of Interest

The authors declare no conflict of interest.

Author Contributions

C.T.K.M., J.H., R.H.A.R., S.G.H., and M.V. designed the experiments. C.T.K.M. conducted the characterization and aging tests (rain simulation, high humidity, and saturated vapor experiments), SEM measurements and analyzed the data. H.A.N. conducted UV/Vis spectroscopy, wetting characterization and data analysis. A.M.S. and G.S.L. carried out AFM measurements and data analysis. D.M. and S.N. fabricated all the devices. N.M. reviewed the first draft of the manuscript. S.G.H. and M.V. conceived the idea and performed initial experiments. C.T.K.M., J.H., and M.V. planned and wrote the manuscript. All authors contributed to data analysis and read and commented on the manuscript.

Data Availability Statement

The data that support the findings of this study are available from the corresponding author upon reasonable request.

Keywords

carbon-based printable perovskite solar cells, condensate formation test, rain falling tests, screen printing, stability, superrepellent coating

Received: January 27, 2024

Revised: April 1, 2024

Published online: May 2, 2024

- [1] A. Kojima, K. Teshima, Y. Shirai, T. Miyasaka, *J. Am. Chem. Soc.* **2009**, *131*, 6050.
- [2] Best Research-Cell Efficiency Chart, <https://www.nrel.gov/pv/cell-efficiency.html> (accessed: April 2024).
- [3] S. Pescetelli, A. Agresti, G. Viskadourous, S. Razza, K. Rogdakis, I. Kalogerakis, E. Spiliariotis, E. Leonardi, P. Mariani, L. Sorbello, M. Pierro, C. Cornaro, S. Bellani, L. Najafi, B. Martín-García, A. E. Del Rio Castillo, R. Oropesa-Nuñez, M. Prato, S. Maranghi, M. L. Parisi, A. Sinicropi, R. Basosi, F. Bonaccorso, E. Kymakis, A. Di Carlo, *Nat. Energy* **2022**, *7*, 597.
- [4] K.-M. Lee, W.-H. Chiu, Y.-H. Tsai, C.-S. Wang, Y.-T. Tao, Y.-D. Lin, *Chem. Eng. J.* **2022**, *427*, 131609.
- [5] E. Berger, M. Bagheri, S. Asgari, J. Zhou, M. Kokkonen, P. Talebi, J. Luo, A. F. Nogueira, T. Watson, S. G. Hashmi, *Sustainable Energy Fuels* **2022**, *6*, 2879.
- [6] C. M. Thi Kim, L. Atourki, M. Ouafi, S. G. Hashmi, *J. Mater. Chem. A* **2021**, *9*, 26650.
- [7] Y. Ma, Q. Zhao, *J. Energy Chem.* **2022**, *64*, 538.
- [8] C. M. T. Kim, M. A. N. Perera, M. Katz, D. Martineau, S. G. Hashmi, *Adv. Eng. Mater.* **2022**, *24*, 2200747.
- [9] Z. Bi, X. Xu, X. Chen, Y. Zhu, C. Liu, H. Yu, Y. Zheng, P. A. Troshin, A. Guerrero, G. Xu, *Chem. Eng. J.* **2022**, *446*, 137164.
- [10] C. Teixeira, P. Spinelli, L. A. Castriotta, D. Müller, S. Öz, L. Andrade, A. Mendes, A. Di Carlo, U. Würfel, K. Wojciechowski, D. Forgács, *Adv. Funct. Mater.* **2022**, *32*, 2206761.
- [11] Y. Cheng, L. Ding, *Energy Environ. Sci.* **2021**, *14*, 3233.
- [12] M. K. Rao, D. N. Sangeetha, M. Selvakumar, Y. N. Sudhakar, M. G. Mahesha, *Sol. Energy* **2021**, *218*, 469.
- [13] S. Mazumdar, Y. Zhao, X. Zhang, *Front. Electron* **2021**, *2*, 712785.
- [14] J. Wei, Q. Wang, J. Huo, F. Gao, Z. Gan, Q. Zhao, H. Li, *Adv. Energy Mater.* **2021**, *11*, 2002326.
- [15] K. Kwak, E. Lim, N. Ahn, J. Heo, K. Bang, S. K. Kim, M. Choi, *Nanoscale* **2019**, *11*, 11369.
- [16] C.-X. Zhang, T. Shen, D. Guo, L.-M. Tang, K. Yang, H.-X. Deng, *Info-Mat* **2020**, *2*, 1034.
- [17] W. Chi, S. K. Banerjee, *Chem. Mater.* **2021**, *33*, 1540.
- [18] W. Chi, S. K. Banerjee, *Chem. Mater.* **2021**, *33*, 4269.
- [19] L. Qiu, K. Xing, J. Zhang, Y. Yang, W. Cao, X. Zhou, K. Zhu, D. Xia, R. Fan, *Adv. Funct. Mater.* **2021**, *31*, 2010368.
- [20] Z. Luo, C. Zhang, L. Yang, J. Zhang, *ChemSusChem* **2022**, *15*, 202102008.
- [21] A. Marmur, C. D. Volpe, S. Siboni, A. Amirfazli, J. W. Drelich, *Surf. Innovations* **2017**, *5*, 3.
- [22] J. Drelich, A. Marmur, *Surf. Innovations* **2014**, *2*, 211.
- [23] S. Zhang, Z. Liu, W. Zhang, Z. Jiang, W. Chen, R. Chen, Y. Huang, Z. Yang, Y. Zhang, L. Han, W. Chen, *Adv. Energy Mater.* **2020**, *10*, 2001610.
- [24] Q. Hu, W. Chen, W. Yang, Y. Li, Y. Zhou, B. W. Larson, J. C. Johnson, Y.-H. Lu, W. Zhong, J. Xu, L. Klivansky, C. Wang, M. Salmeron, A. B. Djurišić, F. Liu, Z. He, R. Zhu, T. P. Russell, *Joule* **2020**, *4*, 1575.
- [25] W. Shi, H. Ye, *J. Phys. Chem. Lett.* **2021**, *12*, 4052.
- [26] M. Li, X. Yan, Z. Kang, Y. Huan, Y. Li, R. Zhang, Y. Zhang, *ACS Appl. Mater. Interfaces* **2018**, *10*, 18787.

- [27] Y. Liu, S. Akin, L. Pan, R. Uchida, N. Arora, J. V. Milić, A. Hinderhofer, F. Schreiber, A. R. Uhl, S. M. Zakeeruddin, A. Hagfeldt, M. I. Dar, M. Grätzel, *Sci. Adv.* **2019**, *5*, eaaw2543.
- [28] S. Daskeviciute-Geguziene, M. A. Truong, K. Rakstys, M. Daskeviciene, R. Hashimoto, R. Murdey, T. Yamada, Y. Kanemitsu, V. Jankauskas, A. Wakamiya, V. Getautis, *ACS Appl. Mater. Interfaces* **2024**, *16*, 1206.
- [29] I. Hwang, I. Jeong, J. Lee, M. J. Ko, K. Yong, *ACS Appl. Mater. Interfaces* **2015**, *7*, 17330.
- [30] H. Zhang, K. Li, M. Sun, F. Wang, H. Wang, A. K.-Y. Jen, *Adv. Energy Mater.* **2021**, *11*, 2102281.
- [31] B. Shi, Y. Li, F. Gao, J. Li, X. Cai, C. Zhang, Y. Wu, C. Lu, J. Wang, S. (Frank) Liu, *Adv. Mater. Interfaces* **2023**, *10*, 2201809.
- [32] Z. Li, J. Dong, C. Liu, J. Guo, L. Shen, W. Guo, *Nano-Micro Lett.* **2019**, *11*, 50.
- [33] S. Xu, L. Zhang, B. Liu, Z. Liang, H. Xu, H. Zhang, J. Ye, H. Ma, G. Liu, X. Pan, *Chem. Eng. J.* **2023**, *453*, 139808.
- [34] M. Vasilopoulou, A. Soultati, P.-P. Filippatos, A. R. B. Mohd Yusoff, M. K. Nazeeruddin, L. C. Palilis, *J. Mater. Chem. C* **2022**, *10*, 11063.
- [35] J. Luo, H. B. Yang, M. Zhuang, S. Liu, L. Wang, B. Liu, *J. Energy Chem.* **2020**, *50*, 332.
- [36] F. Schellenberger, N. Encinas, D. Vollmer, H.-J. Butt, *Phys. Rev. Lett.* **2016**, *116*, 096101.
- [37] H. Xiong, Y. Rui, Y. Li, Q. Zhang, H. Wang, *J. Mater. Chem. C* **2016**, *4*, 6848.
- [38] R. Keshavarzi, N. Molabahrani, N. Afzali, M. Omrani, *Sol. RRL* **2020**, *4*, 2000491.
- [39] S. Abbasi, X. Wang, P. Tipparak, C. Bhoomanee, P. Ruankham, H. Liu, D. Wongratanaphisan, W. Shen, *Mater. Sci. Semicond. Process.* **2023**, *155*, 107241.
- [40] M. J. Hoque, J. Ma, K. F. Rabbi, X. Yan, B. P. Singh, N. V. Upot, W. Fu, J. Kohler, T. S. Thukral, S. Dewanjee, N. Miljkovic, *Appl. Phys. Lett.* **2023**, *123*, 110501.
- [41] Y. A. Mehanna, E. Sadler, R. L. Upton, A. G. Kempchinsky, Y. Lu, C. R. Crick, *Chem. Soc. Rev.* **2021**, *50*, 6569.
- [42] A. Mei, X. Li, L. Liu, Z. Ku, T. Liu, Y. Rong, M. Xu, M. Hu, J. Chen, Y. Yang, M. Grätzel, H. Han, *Science* **2014**, *345*, 295.
- [43] S. G. Hashmi, D. Martineau, M. I. Dar, T. T. T. Myllymäki, T. Sarikka, V. Ulla, S. M. Zakeeruddin, M. Grätzel, *J. Mater. Chem. A* **2017**, *5*, 12060.
- [44] J. V. I. Timonen, M. Latikka, O. Ikkala, R. H. A. Ras, *Nat. Commun.* **2013**, *4*, 2398.
- [45] M. Junaid, H. A. Nurmi, M. Latikka, M. Vuckovac, R. H. A. Ras, *Droplet* **2022**, *1*, 38.
- [46] M. Backholm, D. Molpeceres, M. Vuckovac, H. Nurmi, M. J. Hokkanen, V. Jokinen, J. V. I. Timonen, R. H. A. Ras, *Commun. Mater.* **2020**, *1*, 64.
- [47] N. Gao, F. Geyer, D. W. Pilat, S. Wooh, D. Vollmer, H.-J. Butt, R. Berger, *Nat. Phys.* **2018**, *14*, 191.
- [48] W. Tress, N. Marinova, T. Moehl, S. M. Zakeeruddin, M. K. Nazeeruddin, M. Grätzel, *Energy Environ. Sci.* **2015**, *8*, 995.
- [49] S. Valastro, G. Calogero, E. Smecca, C. Bongiorno, V. Arena, G. Mannino, I. Deretzis, G. Fiscaro, A. L. Magna, A. Alberti, *Sol. RRL* **2024**, *8*, 2300944.
- [50] E. Planes, C. Farha, G. De Moor, S. Narbey, L. Perrin, L. Flandin, *Sol. RRL* **2023**, *7*, 2300492.
- [51] G. De Moor, N. Charvin, C. Farha, T. Meyer, L. Perrin, E. Planes, L. Flandin, *Sol. RRL* **2024**, <https://doi.org/10.1002/solr.202300998>.
- [52] I. Zimmermann, P. Gratia, D. Martineau, G. Grancini, J.-N. Audinot, T. Wirtz, M. K. Nazeeruddin, *J. Mater. Chem. A* **2019**, *7*, 8073.
- [53] Y. Rong, X. Hou, Y. Hu, A. Mei, L. Liu, P. Wang, H. Han, *Nat. Commun.* **2017**, *8*, 14555.
- [54] A. Bashir, J. H. Lew, S. Shukla, D. Gupta, T. Baikie, S. Chakraborty, R. Patidar, A. Bruno, S. Mhaisalkar, Z. Akhter, *Sol. Energy* **2019**, *182*, 225.
- [55] J. You, Y. (Michael) Yang, Z. Hong, T.-B. Song, L. Meng, Y. Liu, C. Jiang, H. Zhou, W.-H. Chang, G. Li, Y. Yang, *Appl. Phys. Lett.* **2014**, *105*, 183902.
- [56] L. Li, H. Rao, Z. Wu, J. Hong, J. Zhang, Z. Pan, X. Zhong, *Adv. Funct. Mater.* **2024**, *34*, 2308428.
- [57] A. J. Barnard, *Proc. R. Soc. London, Ser. A* **1953**, *220*, 132.
- [58] F. P. Incropera, D. P. Dewitt, T. L. Bergman, A. S. Lavine, *Fundamentals of Heat and Mass Transfer*, 6th ed., John Wiley & Sons, New York **2006**.
- [59] M. Thommes, K. Kaneko, A. V. Neimark, J. P. Olivier, F. Rodriguez-Reinoso, J. Rouquerol, K. S. W. Sing, *Pure Appl. Chem.* **2015**, *87*, 1051.
- [60] T. Huhtamäki, X. Tian, J. T. Korhonen, R. H. A. Ras, *Nat. Protoc.* **2019**, *14*, 2259.